



Chirality-2 fermion induced anti-Klein tunneling in a two-dimensional checkerboard latticeJiannan Hua ^{1,2} Z. F. Wang,^{3,4} W. Zhu,^{1,2} and Weiwei Chen ^{5,*}¹*Department of Physics, School of Science, Westlake University, Hangzhou, Zhejiang 310024, China*²*Institute of Natural Sciences, Westlake Institute for Advanced Study, Hangzhou, Zhejiang 310024, China*³*Hefei National Laboratory for Physical Sciences at the Microscale, CAS Key Laboratory of Strongly-Coupled Quantum Matter Physics, Department of Physics, University of Science and Technology of China, Hefei, Anhui 230026, China*⁴*Hefei National Laboratory, University of Science and Technology of China, Hefei, Anhui 230088, China*⁵*Key Laboratory of Intelligent Manufacturing Quality Big Data Tracing and Analysis of Zhejiang Province, College of Science, China Jiliang University, Hangzhou 310018, China*

(Received 17 October 2023; revised 21 January 2024; accepted 4 March 2024; published 22 March 2024)

The quantum tunneling effect in a two-dimensional (2D) checkerboard lattice is investigated. By analyzing the pseudospin texture of the states in a 2D checkerboard lattice based on the low-energy effective Hamiltonian, we find that this system has a chiral symmetry with chirality equal to 2, although compared with regular chiral fermions, its pseudospin orientation does not vary uniformly. This suggests that the perfect reflection chiral tunneling, also known as the anti-Klein tunneling, is expected to appear in a checkerboard lattice as well. To verify the conjecture, we calculate the transmission probability and find that normally incident electron states can be perfectly reflected by the barrier with hole states inside and vice versa. Furthermore, we numerically calculate the tunneling conductance of the checkerboard nanotube using the recursive Green's function method. The results show that a perfect on-off ratio can be achieved by confining the energy of the incident states within a certain range. It also suggests that, by tuning the barrier, the checkerboard nanotube can work as a perfect band filter or tunneling field effect transistor, which transmits electrons selectively with respect to the pseudospin of the incident electrons.

DOI: [10.1103/PhysRevB.109.115429](https://doi.org/10.1103/PhysRevB.109.115429)**I. INTRODUCTION**

Quantum tunneling refers to the passage of particles with finite probability through barriers that are forbidden according to the laws of classical physics [1,2]. Nevertheless, quantum tunneling may bring serious problems when the size of transistors goes down to the nanoscale, e.g., logic errors occur if electrons start tunneling through the barriers when the transistor is off. Therefore, precisely controlling the quantum tunneling effect in the nanoscale transistor is of vital importance for the next-generation electronics [3–10].

Traditional transistors were designed relying on the fundamental charge degree of freedom of electrons, and then the intrinsic spin was also confirmed to modulate the electron transport, giving rise to the study of spintronics [11–13]. Recently, two other degrees of freedom, valley and pseudospin, have been widely investigated in various quantum systems such as monolayer graphene, bilayer graphene, and graphene-based heterojunctions, based on which several types of band filters have been proposed [14–21]. The symmetry consideration is significant in these designing strategies, especially the chiral symmetry in Dirac fermions, which is deeply related to the perfect transmission and perfect reflection in nanostructures [20–24].

In the case of systems with odd chirality, such as monolayer graphene, the normally incident electrons can

completely pass through a barrier of arbitrary height (known as the Klein paradox) [16,25–27]. For systems with even chirality, such as Bernal bilayer graphene [16,27,28], the chiral nature leads to the opposite effect, where electrons are always perfectly reflected for a sufficiently wide barrier for normal incidence, also known as anti-Klein tunneling. However, the perfect reflection in bilayer graphene is only achieved under two-band approximation since an interlayer bias breaks the pseudospin structure [29,30]; therefore, the on-off ratio is low in these materials. Moreover, similar anti-Klein tunneling effects have also been reported in the spin-orbit systems and anisotropic electronic structures [31,32]. Essentially, they all depend on the orientation of spin or pseudospin.

In this paper, we investigate quantum tunneling in a two-dimensional (2D) checkerboard lattice [33–38], where anisotropic chiral symmetry exists. Analyzing the pseudospin texture based on the low-energy effective Hamiltonian, we find that the orientations of the pseudospin and wave vector in this system are locked, and when the angle of the wave vector changes 2π , the angle of the pseudospin changes $2 \times 2\pi$. Additionally, the pseudospin textures of the Fermi surface above and below the touching point are centrosymmetric. These behaviors indicate the existence of chiral symmetry in this system, and the chirality is equal to 2, which suggest that perfect reflection chiral tunneling is expected to appear in a checkerboard lattice as well.

This conjecture of the perfect reflection in the checkerboard lattice is then confirmed by the calculation of transmission probability, which shows that a perfect reflection

*chenweiwei@cjl.u.edu.cn

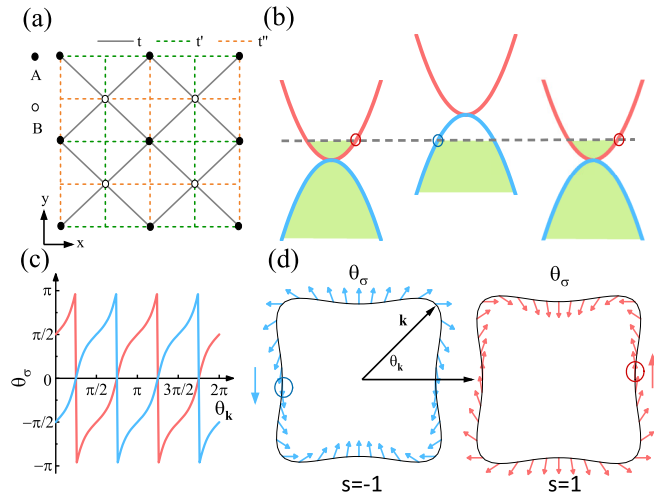


FIG. 1. (a) Checkerboard lattice with nearest- and next-nearest-neighbor hoppings. Two sublattices are labeled by solid and open circles. (b) Schematic diagrams of the band structure and variation of the electrostatic energy caused by the barrier. (c) The angle of pseudospin as a function of the angle of the wave vector: red for subband $s = 1$ and blue for $s = -1$. (d) The textures of pseudospin at the Fermi surface with subband indexes $s = -1$ (blue) and $s = 1$ (red) are denoted by the arrows of unit vectors.

effect for normal incidence is found in the case of $s \neq s'$, where s and s' are the subband indexes inside and outside the barrier, respectively. Inspired by the perfect reflection of normal incidence in the checkerboard lattice, we also suppose that a band filter or tunneling field effect transistor can be designed based on the quasi-one-dimensional checkerboard nanotube. We numerically calculate the tunneling conductance of the checkerboard nanotube using the recursive Green's function method [39,40]. The results show that the current can be entirely blocked by the barrier potential in a certain range. Thus, by tuning the barrier, the checkerboard nanotube can work as a perfect band filter or tunneling field effect transistor, which transmits electrons selectively with respect to the pseudospin of the incident electrons.

Finally, we propose that τ -type organic conductors [41,42] and optical crystals [43] can serve as ideal platforms for creating functional digital devices made of a checkerboard lattice and achieving perfect reflection.

II. MODEL

We start with the tight-binding model of the checkerboard lattice depicted in Fig. 1(a):

$$\begin{aligned}
 H = & - \sum_{i,j} t (a_{i,j}^\dagger b_{i,j} + a_{i,j}^\dagger b_{i,j-1} + a_{i,j}^\dagger b_{i-1,j} + a_{i,j}^\dagger b_{i-1,j-1}) \\
 & + t' (a_{i,j}^\dagger a_{i+1,j} + b_{i,j}^\dagger b_{i,j+1}) + t'' (a_{i,j}^\dagger a_{i,j+1} + b_{i,j}^\dagger b_{i+1,j}) \\
 & + \text{H.c.}, \quad (1)
 \end{aligned}$$

where $a_{i,j}^\dagger$ ($b_{i,j}^\dagger$) and $a_{i,j}$ ($b_{i,j}$) are, respectively, the single electron creation and annihilation operators on the site A (B) of the primitive cell (i, j) , with i (j) being the index along the x (y) direction. Here, t stands for the nearest hopping,

while t' and t'' denote two types of next-nearest hopping. In the calculations below, without loss of generality, we choose the case with $t = t' = -t'' = 1$. A general analysis of parameter settings is provided in Appendix B.

Following the Bloch theorem, the Hamiltonian in the wave vector space reads (details shown in Appendix A)

$$H_{\mathbf{k}} = (-2 \cos \tilde{k}_x + 2 \cos \tilde{k}_y) \sigma_z - 4 \cos \frac{\tilde{k}_x}{2} \cos \frac{\tilde{k}_y}{2} \sigma_x, \quad (2)$$

where $\sigma = (\sigma_x, \sigma_y, \sigma_z)$ is the Pauli matrix of the sublattice pseudospin. The conduction and valence bands of this system quadratically touch at $(\tilde{k}_x, \tilde{k}_y) = (\pi, \pi)$. Thus, we expand the above Hamiltonian around the touching point by redefining the wave vector as $\tilde{k}_x = \pi + k_x$ and $\tilde{k}_y = \pi + k_y$. The low-energy effective Hamiltonian is given by

$$H_{\mathbf{k}} = (k_x^2 - k_y^2) \sigma_z - k_x k_y \sigma_x. \quad (3)$$

The corresponding eigenenergy and eigenstate are

$$E_{\mathbf{k}s} = s k^2 \sqrt{\cos^2 2\theta_{\mathbf{k}} + \frac{1}{4} \sin^2 2\theta_{\mathbf{k}}}. \quad (4)$$

and

$$|\psi_{\mathbf{k}s}\rangle = A_{\mathbf{k}s} \begin{pmatrix} \frac{1}{2} \sin 2\theta_{\mathbf{k}} \\ \cos 2\theta_{\mathbf{k}} - \frac{E_{\mathbf{k}s}}{k^2} \end{pmatrix}. \quad (5)$$

Here, $A_{\mathbf{k}s} = k^2 [2E_{\mathbf{k}s}(E_{\mathbf{k}s} - k^2 \cos 2\theta_{\mathbf{k}})]^{-1/2}$ is the normalization coefficient, $k = |\mathbf{k}|$ and $\theta_{\mathbf{k}} = \arctan(k_y/k_x)$ are the length and angle of \mathbf{k} , respectively, and $s = \pm 1$ denotes different subbands. The pseudospin of this model occurs in the $(x-z)$ plane since the Hamiltonian in Eq. (3) satisfies the anticommutation relation $\{H_{\mathbf{k}}, \sigma_y\} = 0$ [44]. To describe the orientations of the pseudospin and the wave vector in the same plane, we perform a $\frac{\pi}{2}$ rotation along the x direction in the pseudospin space and rewrite the Hamiltonian as

$$\begin{aligned}
 H'_{\mathbf{k}} &= \exp\left(i\sigma_x \frac{\pi}{4}\right) H_{\mathbf{k}} \exp\left(-i\sigma_x \frac{\pi}{4}\right) \\
 &= k^2 \left(\sigma_y \cos 2\theta_{\mathbf{k}} - \frac{1}{2} \sigma_x \sin 2\theta_{\mathbf{k}} \right). \quad (6)
 \end{aligned}$$

Therefore, the angle of pseudospin θ_{σ} is obtained by solving

$$\cos \theta_{\sigma} = \langle \psi'_{\mathbf{k}s} | \sigma_x | \psi'_{\mathbf{k}s} \rangle = \frac{s \sin 2\theta_{\mathbf{k}}}{\sqrt{\sin^2 2\theta_{\mathbf{k}} + 4 \cos^2 2\theta_{\mathbf{k}}}}, \quad (7)$$

$$\sin \theta_{\sigma} = \langle \psi'_{\mathbf{k}s} | \sigma_y | \psi'_{\mathbf{k}s} \rangle = \frac{2s \cos 2\theta_{\mathbf{k}}}{\sqrt{\sin^2 2\theta_{\mathbf{k}} + 4 \cos^2 2\theta_{\mathbf{k}}}}, \quad (8)$$

where $|\psi'_{\mathbf{k}s}\rangle = \exp(i\sigma_x \frac{\pi}{4}) |\psi_{\mathbf{k}s}\rangle$ is the rotated pseudospin state. It is remarkable that the pseudospin angle depends only on the angle of the wave vector, not on the amplitude.

As shown in Figs. 1(c) and 1(d), the angle of the pseudospin varies monotonically with the angle of the wave vector and changes $2 \times 2\pi$ when the wave vector orientation changes 2π . Additionally, the pseudospin textures of the Fermi surface with energy $\pm E$ are centrosymmetric about the touching point. These behaviors are quite similar to chiral fermions with chirality equal to 2, such as Bernal bilayer graphene. The difference is that, in bilayer graphene, the change of the pseudospin angle is always twice the change

of the wave vector angle, while in the case of a checkerboard, θ_σ does not uniformly change with $\theta_{\mathbf{k}}$. This is related to the anisotropic Fermi surface of this model shown in Fig. 1(d).

In the normal incidence condition where $\theta_{\mathbf{k}} = 0$ or π , this anisotropic pseudospin texture does not break the perfect reflection, also called anti-Klein tunneling, reported in the regular 2-chiral fermion. As marked by the red and blue circles in Figs. 1(b) and 1(d), when the states inside and outside the barrier belong to different subbands, the wave functions across the barrier are orthogonal due to the opposite pseudospin orientations, which leads to a perfect reflection if the barrier width tends to infinity, i.e., a potential step.

III. BARRIER POTENTIAL AND TRANSMISSION PROBABILITY

Above, we infer the existence of anti-Klein tunneling in the checkerboard lattice by analyzing the chiral symmetry and pseudospin texture of the low-energy effective Hamiltonian. In the following, we calculate the tunneling transmission probability to address this conjecture. The barrier potential we considered is uniform along the y direction and has a rectangular shape along the x direction:

$$V(x) = \begin{cases} V_s, & 0 \leq x \leq D, \\ 0, & \text{otherwise,} \end{cases} \quad (9)$$

$$\psi_\alpha(x, y) = \exp(ik_y y) \left[\frac{a_\alpha \exp(ik_{\alpha x} x)}{\sqrt{|v(k_{\alpha x})|(1 + |\zeta_{\alpha,1}|^2)}} \begin{pmatrix} 1 \\ \zeta_{\alpha,1} \end{pmatrix} + \frac{b_\alpha \exp(-ik_{\alpha x} x)}{\sqrt{|v(-k_{\alpha x})|(1 + |\zeta_{\alpha,2}|^2)}} \begin{pmatrix} 1 \\ \zeta_{\alpha,2} \end{pmatrix} + \frac{c_\alpha \exp(ik'_{\alpha x} x)}{\sqrt{|v(k'_{\alpha x})|(1 + |\zeta_{\alpha,3}|^2)}} \begin{pmatrix} 1 \\ \zeta_{\alpha,3} \end{pmatrix} + \frac{d_\alpha \exp(-ik'_{\alpha x} x)}{\sqrt{|v(-k'_{\alpha x})|(1 + |\zeta_{\alpha,4}|^2)}} \begin{pmatrix} 1 \\ \zeta_{\alpha,4} \end{pmatrix} \right], \quad (11)$$

where $v(k_{\alpha x}) = \frac{1}{\hbar} \frac{\partial E}{\partial k_x} |_{k_x=k_{\alpha x}}$ is the x component of the quasiparticle velocity. Then we attempt to determine the coefficients. First, $b_R = 0$ since it corresponds to an extra incident wave toward the barrier region. Next, attention is turned to the wave numbers in the incident and transmitting regions. To be specific, it is easy to see that roots $k_{Lx} = k_{Rx} = k_x$ definitely are real, and therefore, modes $\exp(\pm ik_{Lx} x)$ and $\exp(\pm ik_{Rx} x)$ are propagating. However, mathematically, roots k'_{Lx} and k'_{Rx} could be either imaginary or real, which leads to some differences in physics. For the former case, i.e., k'_{Lx} and k'_{Rx} are imaginary just as in bilayer graphene [16], we denote positive real values $\kappa_{Lx} = ik'_{Lx}$, $\kappa_{Rx} = ik'_{Rx}$, and modes $\exp(\pm \kappa_{Lx} x)$, $\exp(\pm \kappa_{Rx} x)$ are therefore evanescent. The convergence of the wave function requires coefficients $d_L = c_R = 0$. In the latter case, i.e., k'_{Lx} and k'_{Rx} are real, modes $\exp(\pm ik'_{Lx} x)$ and $\exp(\pm ik'_{Rx} x)$ are propagating. Here, we choose the signs of k'_{Lx} and k'_{Rx} to satisfy $v(-k'_{Lx}) > 0$ and $v(k'_{Rx}) < 0$, respectively, so that we can also set $d_L = c_R = 0$ for the same reason as $b_R = 0$. So far, for both cases, other coefficients can be obtained by the continuity conditions for both the wave functions and their derivatives. The reflection (R) and transmission (T) probabilities satisfy $R + T = 1$ according to the particle number conservation. To calculate them, it is worth noting

where V_s and D denote the height and length of the barrier, respectively. We assume that the incident wave comes from infinitely away ($x \rightarrow -\infty$) with wave vector $\mathbf{k} = (k_x, k_y)$ and energy E which satisfies the dispersion relation. The wave functions of the system with the barrier can be obtained by solving the equation (details shown in Appendix C):

$$[\hat{H}_{\mathbf{k}} + V(x)]\psi(x, y) = E\psi(x, y). \quad (10)$$

Here, $\hat{H}_{\mathbf{k}}$ serves as an operator in the coordinate representation. It is gotten by redefining the wave vector as $\mathbf{k} = \tilde{\mathbf{k}} - (\pi, \pi)$ in Eq. (2) followed by Fourier transformation between $k_x(k_y)$ and $x(y)$ [45]. Separating variables in Eq. (10) results in $(E - V_\alpha)^2 = 4(\cos k_{\alpha x} - \cos k_y)^2 + 16 \sin^2(k_{\alpha x}/2) \sin^2(k_y/2)$, where the subscript $\alpha = L, M, R$ denotes the incident, barrier, and transmitting regions, respectively. Mathematically, this equation gives two sets of roots, which are denoted by $\pm k_{\alpha x}$ and $\pm k'_{\alpha x}$ and correspond to modes $\exp(\pm ik_{\alpha x} x)$ and $\exp(\pm ik'_{\alpha x} x)$, respectively. Thus, without loss of generality, the solution to Eq. (10) is in the form of

that the incident wave may be scattered into all propagating waves whose velocity components in the x direction are away from the barrier region. Specifically speaking, if the math gives two propagating and two evanescent modes in the incident and transmitting regions, $R = |r|^2$ and $T = |t|^2$, while if the math gives four propagating modes in the incident and transmitting regions, $R = |r|^2 + |r'|^2$ and $T = |t|^2 + |t'|^2$. The settings above make sure that coefficients $r = b_L/a_L$, $r' = c_L/a_L$, $t = a_R/a_L$, and $t' = d_R/a_L$.

Figure 2 shows the transmission probability as a function of the angle of wave vector $\theta = \arctan(k_y/k_x)$ in the case of the incident holelike state with energy $E = -0.1$. We see that the transmission probability is finite (even close to $T = 1$ at some special V_s) and insensitive to the angle for barrier potential with holelike states ($E - V_s < 0$). On the contrary, for the barrier potential with electronlike states ($E - V_s > 0$), the transmission probability is almost zero for the angle $\theta = 0^\circ$, which corresponds to the angle of quasiparticle velocity $\phi = \arctan(\frac{\partial E/\partial k_y}{\partial E/\partial k_x})$ also being zero, i.e., normal incidence. It should be noticed that, under low-energy conditions, these two angles, θ and ϕ , are related by the identity $\tan \phi = \tan \theta \frac{2 \tan^2 \theta - 1}{2 - \tan^2 \theta}$, so the range $\theta \in [-54.7^\circ, 54.7^\circ]$ corresponds to the range $\phi \in [-90^\circ, 90^\circ]$. As a consequence, T is strictly

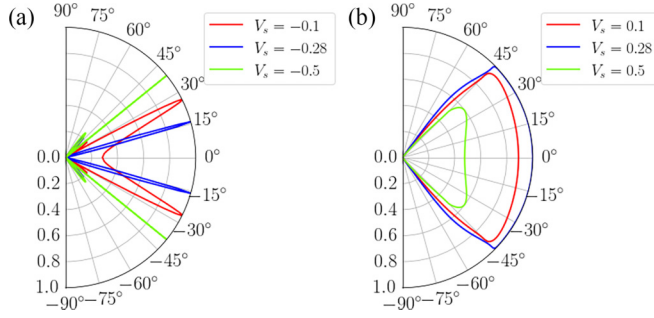


FIG. 2. The angular dependence of the transmission probability in the checkerboard lattice. We set the barrier potential (a) $V_s = -0.50, -0.28, -0.10$ and (b) $V_s = 0.50, 0.28, 0.10$. The incident energy is set to be $E = -0.1$.

0 for $|\theta| \in (54.7^\circ, 90^\circ]$ since the velocity angle of the incident wave exceeds 90° .

For the normal incidence case ($k_y = 0$), we get the analytical form of the transmission probability:

$$T = \begin{cases} \frac{4k_x^2 q_x^2}{4k_x^2 q_x^2 + (k_x^2 - q_x^2)^2 \sin^2(q_x D)}, & \text{if } s = s', \\ \frac{4k_x^2 q_x^2}{4k_x^2 q_x^2 + (k_x^2 + q_x^2)^2 \sinh^2(q_x' D)}, & \text{if } s \neq s', \end{cases} \quad (12)$$

where $s = \text{sgn}(E)$, $s' = \text{sign}(E - V_s)$, $k_x = \arccos(1 - \frac{|E|}{2})$, $q_x = \arccos(1 - \frac{|E - V_s|}{2})$, and $q_x' = \text{arcosh}(1 + \frac{|E - V_s|}{2})$. When the s index (electronlike for $s = +$ or holelike for $s = -$) of the incident state is the same as the states contained in the barrier, Eq. (12) implies that, for certain E and V_s , the transmission probability periodically oscillates with the barrier length D , driven by the $\sin^2(q_x D)$ term. From the physical perspective, constructive interference occurs when $q_x D = N\pi$ ($N \in \mathbb{Z}$), while destructive interference occurs when $q_x D = (N + \frac{1}{2})\pi$ ($N \in \mathbb{Z}$). However, when the s index of the incident state is opposite to the states contained in the barrier, the transmission probability decays exponentially with the barrier length D . Thus, a perfect reflection effect for the normal incidence will be found in the case of $s \neq s'$. These results further confirm the existence of anti-Klein tunneling in this system. Furthermore, this perfect reflection behavior can be achieved in this model within a large window of barrier height than that in AB-stacked bilayer graphene. Once four-band AB-stacked bilayer graphene is considered [46–49], the perfect reflection can only be achieved with the barrier height where the two bands away from the Dirac point do not contribute since an interlayer bias breaks the pseudospin structure [29,30].

IV. TUNNELING CONDUCTANCE

Inspired by the perfect reflection of the normal incidence in the checkerboard lattice, we suppose that a band filter or tunneling field effect transistor can be designed based on the quasi-one-dimensional checkerboard nanotube. The nanotube is assumed to be infinity in the x direction but finite in the y direction with a periodic boundary condition, so k_y is discretized as $k_y = n \frac{2\pi}{M}$, where M is the width of nanotube along the y direction and $n = \frac{M}{2}, \frac{M}{2} - 1, \dots, 0, \dots, -\frac{M}{2} + 1$. Here, we consider the lattice with even widths, which makes

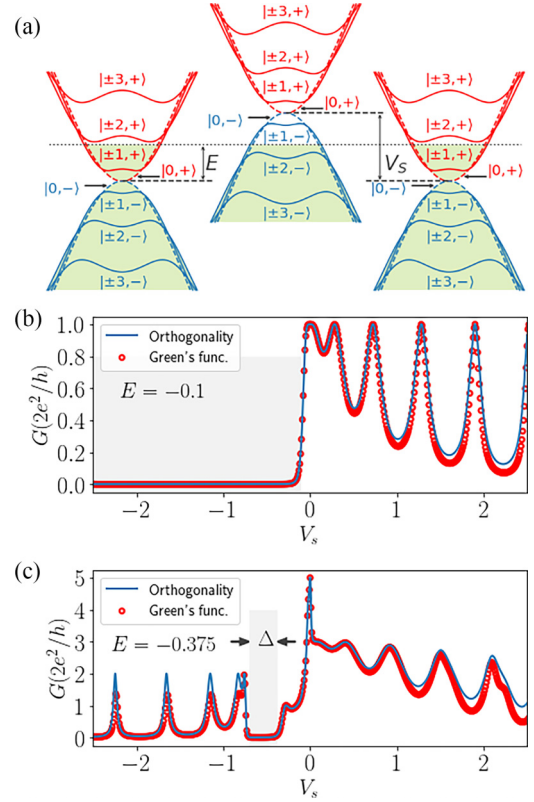


FIG. 3. The tunneling conductance of the checkerboard lattice varies with the height of the barrier V_s . (a) The band structures of the tunneling barrier. The gray regions correspond to the situation that tunneling currents are almost entirely blocked. Incident wave of different energies are calculated: (b) $E_1 = -0.1 \in [-\Delta, 0]$ and (c) $E_2 = -0.375 < -\Delta$. Other parameters $M = 10$, $\Delta = \sqrt{3}(1 - \cos \frac{2\pi}{M}) \approx 0.33$, and $D = 10$. In (b) and (c), the blue solid lines represent the results from the transmission probability calculation (details shown in Appendix C) with the orthogonality assumption of wave functions with different k_y , and the red dots are results from the recursive Green's function.

the band structure gapless. Then we label each subband by (n, s) , as shown in Fig. 3(a). The two lowest bands with index $n = 0$, which correspond to the normally incident states in the 2D checkerboard lattice, touch at $k_x = 0$. Based on the band structure, we define the energy separation between the next-lowest band ($n = \pm 1$) and the quadratic touching point as Δ , and it can be calculated by the width of the lattice as $\Delta = \sqrt{3}(1 - \cos \frac{2\pi}{M})$.

Before calculating the conductance of the checkerboard nanotube with a barrier, we would like to analyze the orthogonality of the wave functions of different slices (assemblages of all primitive cells with the same x) in the nanotube since the wave propagates slice by slice. The slice wave function can be expressed by Eq. (5) as $\Psi_{n,s,k_x}(x) = \frac{1}{\sqrt{M}} [\psi_{n,s,k_x}(x, y_1), \dots, \psi_{n,s,k_x}(x, y_M)]^T$, where k_y is replaced by n . The wave functions of the two lowest bands take

$$\psi_{0,+k_x}(\mathbf{r}) = \begin{pmatrix} 1 \\ 0 \end{pmatrix} \exp(ik_x x), \quad (13)$$

$$\psi_{0,-k_x}(\mathbf{r}) = \begin{pmatrix} 0 \\ 1 \end{pmatrix} \exp(ik_x' x). \quad (14)$$

where $\psi_{0,+k_x}(\mathbf{r})$ only populates sublattice A and $\psi_{0,-k_x}(\mathbf{r})$ only populates sublattice B, which is like the zero-mode solution of the Dirac fermions in a magnetic field [50]. Thus, one can get

$$\Psi_{0,+k_x}^\dagger(x)\Psi_{0,-k_x}(x) = \sum_y \psi_{0,+k_x}^\dagger(\mathbf{r})\psi_{0,-k_x}(\mathbf{r}) = 0. \quad (15)$$

Additionally, the slice wave functions with different band index n are also orthogonal due to

$$\Psi_{n,s,k_x}^\dagger(x)\Psi_{n',s',k_x'}(x) \propto \sum_y \exp[i(k_y - k_y')y] = \delta_{k_y,k_y'} = \delta_{n,n'}. \quad (16)$$

Combining the relations in Eqs. (15) and (16), it is easy to see that slice wave function $\Psi_{0,s,k_x}(x)$ is orthogonal to all other slice wave functions $\Psi_{n,s',k_x'}(x)$, with $s' \neq s$. In other words, slice wave functions with energies in the range $E \in [0, \Delta]$ ($E \in [-\Delta, 0]$) are orthogonal to those in the range $E < 0$ ($E > 0$), which implies that an incident electronlike wave with energy $E \in [0, \Delta]$ cannot tunnel through a potential barrier with holelike states inside, and similarly, an incident hole wave with energy $E \in [-\Delta, 0]$ cannot tunnel through a potential barrier with electron states inside. This is consistent with the anti-Klein tunneling we find under the normal incidence condition. Additionally, it is worth pointing out that, for the evanescent wave, i.e., k_x is imaginary, although the state does not appear in the dispersion relation, Fig. 3(a), orthogonality relations in Eqs. (15) and (16) still hold if the subscript n is replaced with corresponding transverse wave number $k_y = n \frac{2\pi}{M}$.

To verify the perfect reflection in the checkerboard nanotube, we calculate the tunneling conductance in two ways. One is to sum transmission probabilities over all channels obtained in the previous section, i.e., $G \approx \frac{2e^2}{h} \sum_{n=-M/2}^{M/2-1} T_n$, where n represents the corresponding transverse wave number k_y , as previously mentioned. The other is to use the zero-bias Landauer formula combined with the recursive Green's function method [39,40].

Figure 3 also reports results of the tunneling conductance G vs the height of barrier V_s with transverse width $M = 10$, length $D = 10$, and incident energies (b) $E_1 = -0.1$ and (c) $E_2 = -0.375$. In this condition, the energy separation between the band $n = \pm 1$ and $n = 0$ is $\Delta \approx 0.33$, so the incident state with energy $E_1 \in [-\Delta, 0]$ contains only contribution from band $(0, -)$, while the incident state with energy $E_2 < -\Delta$ also contains contribution from band $n \neq 0$.

For the incident holelike state with energy E_1 , as shown in Fig. 3(b), the current is almost entirely blocked by the barrier potential when $E_1 - V_s > 0$, in which the barrier contains electronlike states inside, and performs resonant tunneling in the other range. For the incident energy E_2 , shown in Fig. 3(c), the current is blocked by the barrier with height $V_s \in (E_2 - \Delta, E_2)$, which contains states from band $(0, +)$, and tunnels through the barrier resonantly in the other range. These results are in good agreement with our predictions from orthogonality analysis of wave functions and imply that a barrier potential in the checkerboard lattice can play the role of a band filter: When chemical potential E is tuned to be in the

range $[-\Delta, 0]$, the negative barrier potential blocks the electronlike states tunneling, while the positive barrier transmits these states. In addition, the peaks and valleys in Fig. 3(b) reflect the transmission enhancement from the resonances due to the constructive interference and the transmission suppression from the antiresonances due to the destructive interference inside the barrier, respectively. This is consistent with the $\sin^2(q_x D)$ term in the case $s = s'$ of Eq. (12).

From the comparison of results from these two methods, it can be seen that the tunneling conductance is insensitive to the bands coupling, especially in the perfect reflection region, which meets the expectation from the slice wave function analysis that $\Psi_{0,\pm,k_x}(x)$ and $\Psi_{n,\mp,k_x'}(x)$ are completely orthogonal. Another remarkable behavior found in tunneling conductance is the presence of many resonance peaks during the change of V_s , at which the barrier is transparent to one or more channels. These resonance peaks arise from waves that are reflected multiple times in the barrier and then transmitted in the same phase, which is like that taking place in the optical Fabry-Perot resonator or in a microwave capacitively coupled transmission-line resonator [51]. This can be proven by that, in Fig. 3(b), the locations of resonance peaks are well matched to the resonance condition of transmission probability for the normal incidence, i.e., $q_x D = \pi N$.

V. MATERIALS REALIZATION

So far, we have explored the perfect reflection Klein tunneling in the checkerboard lattice based on the tight-binding model. Then we suggest some experimental systems where our simulation results can be potentially observed. At first, attention can be paid to the τ -type organic conductors, in each conducting layer of which donor molecules form a square lattice and anion molecules are arranged on it with a checkerboard pattern [41,42]. The fact that the conduction and valence bands exhibit the quadratic band touching at the corner of the square Brillouin zone was also confirmed by the tight-binding model and density functional theory (DFT) calculations. Additionally, the optical checkerboard-like lattices with cold atoms are compelling candidates to simulate this condensed-matter problem due to the simple tuning of the parameters [43]. Lattice constants of these material candidates $a \lesssim 1$ nm. From the results shown in Fig. 3 and Appendix D, it is evident that, when the gate width is < 10 times lattice constants, the transmission in the anti-Klein region already approaches zero to an extreme extent, indicating that the contribution from evanescent waves is almost negligible. Therefore, it is obvious that using gate widths comparable with or even smaller than existing tunneling field effect transistors ($\gtrsim 10$ nm) [52,53] can completely achieve perfect reflection.

VI. CONCLUSION AND DISCUSSION

In summary, we have studied the electronic quantum tunneling of a checkerboard lattice through a barrier potential. Due to the chiral nature of the quasiparticles, we find that there exists anti-Klein tunneling, which leads to the perfect reflection of the normally incident waves. Moreover, we have

also shown that a barrier potential can play the role of a band filter or tunneling field effect transistor in the checkerboard nanotube, which transmits the electronic states according to the selection rule. Finally, we expect that the checkerboard lattice can be realized in materials like τ -type organic conductors and optical checkerboardlike lattices.

ACKNOWLEDGMENTS

This paper was supported by Pioneer and Leading Goose R&D Program of Zhejiang (Grant No. 2022SDXHDX0005) and the Key R&D Program of Zhejiang Province (Grant No. 2021C01002).

APPENDIX A: TIGHT-BINDING MODEL

The tight-binding model of the checkerboard lattice depicted in Fig. 1(a) is

$$H = - \sum_{i,j} t (a_{i,j}^\dagger b_{i,j} + a_{i,j}^\dagger b_{i,j-1} + a_{i,j}^\dagger b_{i-1,j} + a_{i,j}^\dagger b_{i-1,j-1}) + t' (a_{i,j}^\dagger a_{i+1,j} + b_{i,j}^\dagger b_{i,j+1}) + t'' (a_{i,j}^\dagger a_{i,j+1} + b_{i,j}^\dagger b_{i+1,j}) + \text{H.c.}, \quad (\text{A1})$$

where $a_{i,j}^\dagger (b_{i,j}^\dagger)$ and $a_{i,j} (b_{i,j})$ are, respectively, the single electron creation and annihilation operator on the site $A(B)$ of the primitive cell (i, j) , with $i(j)$ being the index along the $x(y)$ direction. Here, t stands for the nearest hopping, while t' and t'' denote two types of next-nearest hopping. To get the Hamiltonian in the wave vector space, apply the Fourier transform:

$$\hat{c}_{i,j} = \frac{1}{\sqrt{\mathcal{V}}} \sum_{\mathbf{k}} \exp(i\mathbf{k} \cdot \mathbf{r}_{i,j}^c) \hat{c}_{\mathbf{k}}, \quad (\text{A2})$$

where \mathcal{V} is the area of the lattice, and c represents either a or b , and $\mathbf{r}_{i,j}^c$ is the position of the corresponding sublattice of the primitive cell (i, j) . In this paper, we take the length of the primitive translation vectors as the unit length, which is also the distance of the next-nearest hopping. Then $\mathbf{r}_{i,j}^a = (i, j)$, $\mathbf{r}_{i,j}^b = (i + \frac{1}{2}, j + \frac{1}{2})$. Each item in Eq. (A1) is in the form:

$$\begin{aligned} \sum_{i,j} \hat{c}_{i,j}^\dagger \hat{c}_{i+\delta i, j+\delta j} &= \frac{1}{\mathcal{V}} \sum_{i,j} \sum_{\mathbf{k}, \mathbf{k}'} \exp(-i\mathbf{k} \cdot \mathbf{r}_{i,j}^c) \hat{c}_{\mathbf{k}}^\dagger \exp(i\mathbf{k}' \cdot \mathbf{r}_{i+\delta i, j+\delta j}^c) \hat{c}_{\mathbf{k}'} \\ &= \frac{1}{\mathcal{V}} \sum_{\mathbf{k}, \mathbf{k}'} \sum_{i,j} \exp[i(\mathbf{k}' - \mathbf{k}) \cdot \mathbf{r}_{i,j}^c] \exp(i\mathbf{k}' \cdot \delta \mathbf{r}) \hat{c}_{\mathbf{k}}^\dagger \hat{c}_{\mathbf{k}'} \\ &= \sum_{\mathbf{k}} \exp(i\mathbf{k} \cdot \delta \mathbf{r}) \hat{c}_{\mathbf{k}}^\dagger \hat{c}_{\mathbf{k}}, \end{aligned} \quad (\text{A3})$$

where $\delta \mathbf{r} = \mathbf{r}_{i+\delta i, j+\delta j}^c - \mathbf{r}_{i,j}^c$. Thus, Eq. (A1) becomes

$$\begin{aligned} \hat{H} &= - \sum_{\mathbf{k}} \left(t \left\{ \exp \left[i\tilde{\mathbf{k}} \cdot \left(\frac{1}{2}, \frac{1}{2} \right) \right] + \exp \left[i\tilde{\mathbf{k}} \cdot \left(\frac{1}{2}, -\frac{1}{2} \right) \right] + \exp \left[i\tilde{\mathbf{k}} \cdot \left(-\frac{1}{2}, \frac{1}{2} \right) \right] + \exp \left[i\tilde{\mathbf{k}} \cdot \left(-\frac{1}{2}, -\frac{1}{2} \right) \right] \right\} \hat{a}_{\mathbf{k}}^\dagger \hat{b}_{\mathbf{k}} \right. \\ &\quad \left. + \{ t' \exp[i\tilde{\mathbf{k}} \cdot (1, 0)] + t'' \exp[i\tilde{\mathbf{k}} \cdot (0, 1)] \} \hat{a}_{\mathbf{k}}^\dagger \hat{a}_{\mathbf{k}} + \{ t'' \exp[i\tilde{\mathbf{k}} \cdot (1, 0)] + t' \exp[i\tilde{\mathbf{k}} \cdot (0, 1)] \} \hat{b}_{\mathbf{k}}^\dagger \hat{b}_{\mathbf{k}} \right) + \text{H.c.} \\ &= - \sum_{\mathbf{k}} 4t \cos \frac{\tilde{k}_x}{2} \cos \frac{\tilde{k}_y}{2} (\hat{a}_{\mathbf{k}}^\dagger \hat{b}_{\mathbf{k}} + \text{H.c.}) + 2(t' \cos \tilde{k}_x + t'' \cos \tilde{k}_y) \hat{a}_{\mathbf{k}}^\dagger \hat{a}_{\mathbf{k}} + 2(t'' \cos \tilde{k}_x + t' \cos \tilde{k}_y) \hat{b}_{\mathbf{k}}^\dagger \hat{b}_{\mathbf{k}} \\ &= \sum_{\mathbf{k}} \hat{c}_{\mathbf{k}}^\dagger H_{\mathbf{k}} \hat{c}_{\mathbf{k}}, \end{aligned} \quad (\text{A4})$$

where $\hat{c}_{\mathbf{k}} = \begin{pmatrix} \hat{a}_{\mathbf{k}} \\ \hat{b}_{\mathbf{k}} \end{pmatrix}$, $H_{\mathbf{k}} = -2 \begin{pmatrix} t' \cos \tilde{k}_x + t'' \cos \tilde{k}_y & 2t \cos \frac{\tilde{k}_x}{2} \cos \frac{\tilde{k}_y}{2} \\ 2t \cos \frac{\tilde{k}_x}{2} \cos \frac{\tilde{k}_y}{2} & t'' \cos \tilde{k}_x + t' \cos \tilde{k}_y \end{pmatrix}$.

APPENDIX B: PARAMETER ANALYSIS AND τ -TYPE ORGANIC CONDUCTOR

As shown in Appendix A, the wave vector space form of the Hamiltonian in Eq. (1) with arbitrary parameters t , t' , and t'' is given by

$$\begin{aligned} H_{\mathbf{k}} &= -2 \begin{pmatrix} t' \cos \tilde{k}_x + t'' \cos \tilde{k}_y & 2t \cos \frac{\tilde{k}_x}{2} \cos \frac{\tilde{k}_y}{2} \\ 2t \cos \frac{\tilde{k}_x}{2} \cos \frac{\tilde{k}_y}{2} & t'' \cos \tilde{k}_x + t' \cos \tilde{k}_y \end{pmatrix} \\ &= -(t' + t'')(\cos \tilde{k}_x + \cos \tilde{k}_y) \sigma_0 - (t' - t'')(\cos \tilde{k}_x - \cos \tilde{k}_y) \sigma_z - 4t \cos \frac{\tilde{k}_x}{2} \cos \frac{\tilde{k}_y}{2} \sigma_x, \end{aligned} \quad (\text{B1})$$

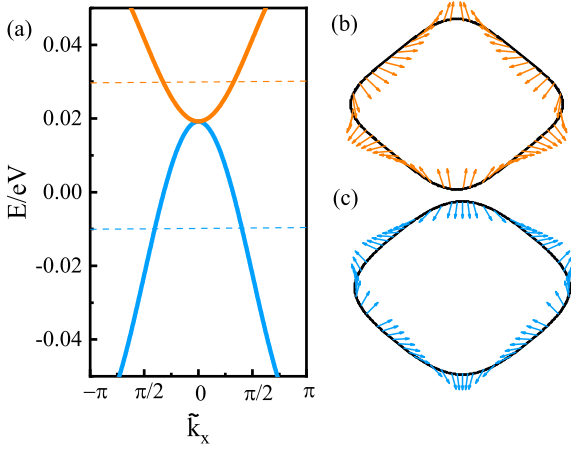


FIG. 4. (a) Band structure of the Hamiltonian with parameters obtained by density functional theory (DFT) fitting of τ -type organic conductor. We set $\tilde{k}_y = \pi$. (b) and (c) Textures of pseudospin at the Fermi surfaces $E_f = 0.03$ eV (orange) and $E_f = -0.01$ eV (blue), respectively.

where σ_0 is the identity matrix. The corresponding dispersion relation is

$$E_{\tilde{k}_{\pm}} = -(t' + t'')(\cos \tilde{k}_x + \cos \tilde{k}_y) \pm \sqrt{(t' - t'')^2(\cos \tilde{k}_x - \cos \tilde{k}_y)^2 + 16t^2 \cos^2 \frac{\tilde{k}_x}{2} \cos^2 \frac{\tilde{k}_y}{2}}. \quad (\text{B2})$$

The parameters $t = t' = -t'' = 1$ set in the main text are a showcase without loss of generality based on following reasons. First, since the σ_0 term in the Hamiltonian in Eq. (B1) does not affect the expression of the eigenstates, the choice $t' = -t''$ does not affect the orientation of the pseudospin, which is the essential reason for Klein and anti-Klein

tunneling. Secondly, from the dispersion relation Eq. (B2), it is obvious that the location of the touching point $\tilde{\mathbf{k}} = (\pi, \pi)$ is independent of the values of t , t' , and t'' . Thirdly, we performed the calculation of the pseudospin texture of the model with parameters obtained by DFT calculation of the τ -type organic conductor reported in Ref. [42], which gives $t = 0.16$ eV, $t' = 0.13t$, and $t'' = -0.07t$. As shown in Figs. 4(b) and 4(c), we find that, when the orientation of wave vector changes 2π in the $(x-y)$ plane, the orientation of pseudospin changes $2 \times 2\pi$ in the $(x-z)$ plane. In Figs. 4(b) and 4(c), the z axis of the pseudospin coincides with the y axis of the wave vector. This implies that the values of t , t' , and t'' can affect the energy level of the touching point and the shape of the Fermi surface but do not change the nature of the system, which is a chirality-2 fermion. Finally, for the normal incidence $\tilde{k}_y = \pi$, the off-diagonal components vanish. Hence, the system holds two \tilde{k}_x -independent orthogonal eigenstates $\begin{pmatrix} 0 \\ 1 \end{pmatrix}$ and $\begin{pmatrix} 1 \\ 0 \end{pmatrix}$, the same as in Eq. (13), which directly induce anti-Klein tunneling.

APPENDIX C: CALCULATION OF TRANSMISSION PROBABILITY

1. Determining the wave modes

Before solving Eq. (10) globally, we need to determine the modes of the wave function in each region. Without loss of generality, we suppose the wave function as $\psi(x, y) = \begin{pmatrix} \zeta_A \\ \zeta_B \end{pmatrix} \exp(\lambda_x x) \exp(\lambda_y y)$ and substitute it into Eq. (10):

$$\hat{H}_{\mathbf{k}} \begin{pmatrix} \zeta_A \\ \zeta_B \end{pmatrix} \exp(\lambda_x x) \exp(\lambda_y y) = E' \begin{pmatrix} \zeta_A \\ \zeta_B \end{pmatrix} \exp(\lambda_x x) \exp(\lambda_y y), \quad (\text{C1})$$

where $E' = E - V$, and $\hat{H}_{\mathbf{k}}$ is gotten by redefining the wave vector as $\mathbf{k} = \tilde{\mathbf{k}} - (\pi, \pi)$ in Eq. (2) followed by Fourier transformation between $k_x(k_y)$ and $x(y)$ [45] to serve as an operator in the coordinate representation. Therefore, we get

$$\begin{pmatrix} 2[\cos(i\lambda_x) - \cos(i\lambda_y)] & -4 \sin \frac{i\lambda_x}{2} \sin \frac{i\lambda_y}{2} \\ -4 \sin \frac{i\lambda_x}{2} \sin \frac{i\lambda_y}{2} & 2[-\cos(i\lambda_x) + \cos(i\lambda_y)] \end{pmatrix} \begin{pmatrix} \zeta_A \\ \zeta_B \end{pmatrix} \exp(\lambda_x x) \exp(\lambda_y y) = E' \begin{pmatrix} \zeta_A \\ \zeta_B \end{pmatrix} \exp(\lambda_x x) \exp(\lambda_y y). \quad (\text{C2})$$

Calculating

$$\det \begin{vmatrix} 2[\cos(i\lambda_x) - \cos(i\lambda_y)] - E' & -4 \sin \frac{i\lambda_x}{2} \sin \frac{i\lambda_y}{2} \\ -4 \sin \frac{i\lambda_x}{2} \sin \frac{i\lambda_y}{2} & 2[-\cos(i\lambda_x) + \cos(i\lambda_y)] - E' \end{vmatrix} = 0 \quad (\text{C3})$$

leads to

$$E'^2 = 4(u - v)^2 + 4(1 - u)(1 - v), \quad (\text{C4})$$

where auxiliary values

$$u \equiv \cos(i\lambda_x) = \begin{cases} \cos k_x & \text{for } \lambda_x = ik_x \text{ is imaginary,} \\ \cosh k_x & \text{for } \lambda_x = k_x \text{ is real,} \end{cases} \quad (\text{C5})$$

$$v \equiv \cos(i\lambda_y) = \cos k_y \text{ for } \lambda_y = ik_y \text{ is imaginary.}$$

Rewriting Eq. (C4) as a quadratic equation with u as the variable,

$$u^2 - (1 + v)u + \left(v^2 - v + 1 - \frac{E'^2}{4}\right) = 0. \quad (\text{C6})$$

The solution is

$$u_{\pm} = \frac{1 + v \pm \sqrt{E'^2 - 3(1 - v)^2}}{2}. \quad (\text{C7})$$

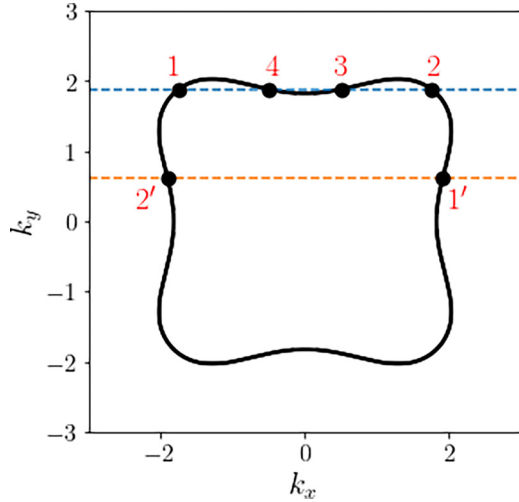


FIG. 5. The black curve is a typical Fermi surface of the checkerboard lattice for $t = t' = -t'' = 1$. Specifically, here, $E' = 2.5$. The orange and blue lines correspond to $k_y = \frac{3\pi}{5}$ and $\frac{\pi}{5}$, respectively. The black curve and the orange line intersect at points 1' and 2', which represent propagating modes of the same group. The black curve and the blue line intersect at points 1, 2, 3, and 4, which represent propagating modes belonging to two groups.

Additionally, Eq. (C4) leads to that the necessary and sufficient condition for $\frac{\partial E'^2}{\partial u} > 0$ is $u > \frac{1+v}{2}$. As a consequence, mathematically, for a certain v , E'^2 is monotonically decreasing for $u \in (-\infty, \frac{v+1}{2})$ and monotonically increasing for $u \in (\frac{v+1}{2}, +\infty)$. Thus, E'^2 achieves a minimum value $3(1-v)^2$ when $u = \frac{v+1}{2}$. Additionally, $E'^2 = 4(1-v)^2$ for $u = 1$. These result in, physically, for $|E'| < \sqrt{12}$ and a fixed $v \in [-1, 1]$:

(1) If $|E'| < \sqrt{3}(1-v)$, there is not any mode.

(2) If $\sqrt{3}(1-v) < |E'| < 2(1-v)$, just shown as the blue line in the Fig. 5, there are four modes with

$$\begin{aligned} \lambda_x &= \pm ik_x = \pm i \arccos(u_-), & \text{propagating,} \\ \lambda_x &= \pm ik_x = \pm i \arccos(u_+), & \text{propagating,} \end{aligned} \quad (\text{C8})$$

and the transmission probability is easy to be calculated, as introduced in Appendix C 3.

(3) If $|E'| > 2(1-v)$, just shown as the orange line in the Fig. 5, there are four modes with

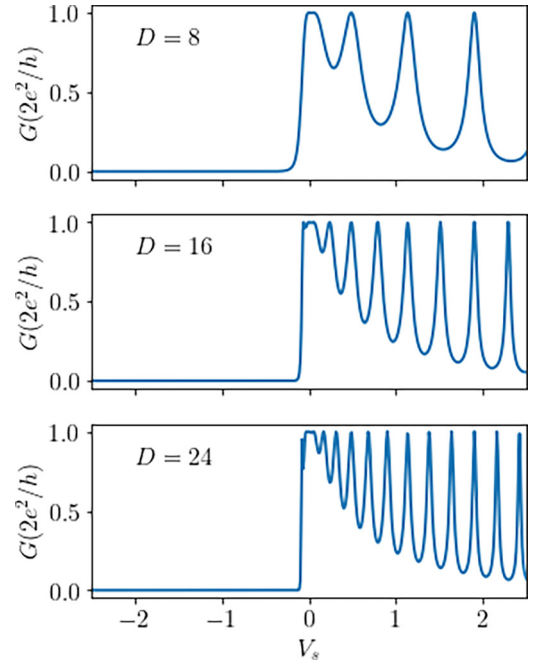


FIG. 6. The zero temperature linear tunneling conductance of the checkerboard lattice varies with the height V_s and width D of the barrier. Incident wave energy $E = -0.1 \in [-\Delta, 0]$. Other parameters $M = 10$, $\Delta = \sqrt{3}(1 - \cos \frac{2\pi}{M}) \approx 0.33$, $D = 8$ (top panel), $D = 16$ (middle panel), and $D = 24$ (bottom panel).

$$\begin{aligned} \lambda_x &= \pm ik_x = \pm i \arccos(u_-), & \text{propagating,} \\ \lambda_x &= \pm k_x = \pm \text{arcosh}(u_+), & \text{evanescent,} \end{aligned} \quad (\text{C9})$$

and the transmission probability is easy to be calculated, as introduced in Appendix C 2.

So far, for certain $E' = E - V$ and k_y , Eq. (10) gives two sets of roots in each region, which are denoted by $\pm k_{\alpha x}$ and $\pm k'_{\alpha x}$ and correspond to modes $\exp(\pm ik_{\alpha x}x)$ and $\exp(\pm ik'_{\alpha x}x)$, respectively. The subscript $\alpha = L, M, R$ denotes the incident, barrier, and transmitting regions, respectively. Next, we discuss the instances of Eq. (11) in different scenarios. As we will show later that modes in the barrier do not affect the way of solving the wave function, we classify the scenarios by the modes (mathematically) in the incident and transmitting regions.

2. Scenario of two propagating modes and two evanescent modes

In the scenario that two propagating modes and two evanescent modes (mathematically) exist in both sides of the barrier, the wave function Eq. (11) becomes

$$\psi(x, y) = e^{ik_y y} \begin{cases} \left(\frac{1}{\zeta_1^L} \exp(\lambda_1^L x) + r \left(\frac{1}{\zeta_2^L} \exp(\lambda_2^L x) + c' \left(\frac{1}{\zeta_3^L} \exp(\lambda_3^L x) \right) \right), & x < 0, \\ a \left(\frac{1}{\zeta_1^M} \exp(\lambda_1^M x) + b \left(\frac{1}{\zeta_2^M} \exp(\lambda_2^M x) + c \left(\frac{1}{\zeta_3^M} \exp(\lambda_3^M x) + d \left(\frac{1}{\zeta_4^M} \exp(\lambda_4^M x) \right) \right) \right), & 0 \leq x \leq D, \\ t \left(\frac{1}{\zeta_1^L} \exp(\lambda_1^L x) + d' \left(\frac{1}{\zeta_4^L} \exp(\lambda_4^L x) \right) \right), & D < x. \end{cases} \quad (\text{C10})$$

where the superscripts L, M, R denote the incident (left), barrier (medial), and transmitting (right) regions, respectively. Note, since $V(x)$ has the same value for the incident (L) and transmitting (R) regions, the pseudospin states in the transmitting (R) region have been represented by ones in the incident (L) region. For pseudospin states $(\zeta_{1/2/3/4}^L)$, subscript 1(2) corresponds to the propagating wave with a positive (negative) component of velocity in the x direction $v_x \equiv \frac{1}{\hbar} \frac{\partial E}{\partial k_x}$, while 3(4) corresponds to the evanescent wave with a positive (negative) wave number λ_x in the x direction, respectively.

Considering the continuity of both the wave function in Eq. (C10) and its partial derivative $\partial_x \psi(x, y)$ respectively at $x = 0$, we have $[\psi(x, y)]_{x \rightarrow 0^-} = [\psi(x, y)]_{x \rightarrow 0^+}$ and $[\partial_x \psi(x, y)]_{x \rightarrow 0^-} = [\partial_x \psi(x, y)]_{x \rightarrow 0^+}$. Similarly, at $x = D$, we

have $[\psi(x, y)]_{x \rightarrow D^-} = [\psi(x, y)]_{x \rightarrow D^+}$ and $[\partial_x \psi(x, y)]_{x \rightarrow D^-} = [\partial_x \psi(x, y)]_{x \rightarrow D^+}$. These four equations can be simplified to be

$$P \begin{pmatrix} 1 \\ r \\ c' \end{pmatrix} = M \begin{pmatrix} a \\ b \\ c \\ d \end{pmatrix}, \quad (\text{C11})$$

and

$$M \Lambda \begin{pmatrix} a \\ b \\ c \\ d \end{pmatrix} = Q \begin{pmatrix} t \\ d' \end{pmatrix}, \quad (\text{C12})$$

where

$$P \equiv \begin{pmatrix} 1 & 1 & 1 \\ \zeta_1^L & \zeta_2^L & \zeta_3^L \\ \lambda_1^L & \lambda_2^L & \lambda_3^L \\ \zeta_1^L \lambda_1^L & \zeta_2^L \lambda_2^L & \zeta_3^L \lambda_3^L \end{pmatrix}, \quad M \equiv \begin{pmatrix} 1 & 1 & 1 & 1 \\ \zeta_1^M & \zeta_2^M & \zeta_3^M & \zeta_4^M \\ \lambda_1^M & \lambda_2^M & \lambda_3^M & \lambda_4^M \\ \zeta_1^M \lambda_1^M & \zeta_2^M \lambda_2^M & \zeta_3^M \lambda_3^M & \zeta_4^M \lambda_4^M \end{pmatrix}, \quad \Lambda \equiv \begin{pmatrix} e^{\lambda_1^M D} & 0 & 0 & 0 \\ 0 & e^{\lambda_2^M D} & 0 & 0 \\ 0 & 0 & e^{\lambda_3^M D} & 0 \\ 0 & 0 & 0 & e^{\lambda_4^M D} \end{pmatrix},$$

$$Q \equiv \begin{pmatrix} e^{\lambda_1^L D} & e^{\lambda_4^L D} \\ \zeta_1^L e^{\lambda_1^L D} & \zeta_4^L e^{\lambda_4^L D} \\ \lambda_1^L e^{\lambda_1^L D} & \lambda_4^L e^{\lambda_4^L D} \\ \zeta_1^L \lambda_1^L e^{\lambda_1^L D} & \zeta_4^L \lambda_4^L e^{\lambda_4^L D} \end{pmatrix}.$$

The combination of Eqs. (C11) and (C12):

$$M^{-1} P \begin{pmatrix} 1 \\ r \\ c' \end{pmatrix} = \begin{pmatrix} a \\ b \\ c \\ d \end{pmatrix} = \Lambda^{-1} M^{-1} Q \begin{pmatrix} t \\ d' \end{pmatrix}, \quad (\text{C13})$$

is a linear relation from which we can easily get parameters r, t . Thus, the reflection (R) and transmission (T) probabilities can be calculated as $R = |r|^2$ and $T = |t|^2$.

3. Scenario of four propagating modes

In the scenario that four propagating modes exist in both sides of the barrier, the scattering happening between modes with different magnitudes of velocities should be considered. To change the algorithm as little as possible, we denote $\lambda_1^L = ik_x$, $\lambda_2^L = -ik_x$, $\lambda_3^L = ik'_x$, and $\lambda_4^L = -ik'_x$. The wave function in Eq. (11) becomes

$$\psi(x, y) = \exp(ik_y y) \begin{cases} \frac{1}{\sqrt{|v_x|}} \alpha_{1,2} \begin{pmatrix} 1 \\ \zeta_1^L \end{pmatrix} \exp(\lambda_1^L x) + \frac{r}{\sqrt{|v_x|}} \alpha_{1,2} \begin{pmatrix} 1 \\ \zeta_2^L \end{pmatrix} \exp(\lambda_2^L x) + \frac{r'}{\sqrt{|v'_x|}} \alpha_{3,4} \begin{pmatrix} 1 \\ \zeta_4^L \end{pmatrix} \exp(\lambda_4^L x), & x < 0, \\ a' \begin{pmatrix} 1 \\ \zeta_1^M \end{pmatrix} \exp(\lambda_1^M x) + b' \begin{pmatrix} 1 \\ \zeta_2^M \end{pmatrix} \exp(\lambda_2^M x) + c' \begin{pmatrix} 1 \\ \zeta_3^M \end{pmatrix} \exp(\lambda_3^M x) + d' \begin{pmatrix} 1 \\ \zeta_4^M \end{pmatrix} \exp(\lambda_4^M x), & 0 \leq x \leq D, \\ \frac{t}{\sqrt{|v_x|}} \alpha_{1,2} \begin{pmatrix} 1 \\ \zeta_1^L \end{pmatrix} \exp(\lambda_1^L x) + \frac{t'}{\sqrt{|v'_x|}} \alpha_{3,4} \begin{pmatrix} 1 \\ \zeta_3^L \end{pmatrix} \exp(\lambda_3^L x), & D < x. \end{cases} \quad (\text{C14})$$

where $\alpha_{1,2} = \frac{1}{\sqrt{1+|\zeta_1^L|^2}} = \frac{1}{\sqrt{1+|\zeta_2^L|^2}}$ and $\alpha_{3,4} = \frac{1}{\sqrt{1+|\zeta_3^L|^2}} = \frac{1}{\sqrt{1+|\zeta_4^L|^2}}$ are normalization constants. Comparing with Eq. (C10), $(\zeta_{3/4}^L)$ here are propagating modes, and subscript 3(4) corresponds to the positive (negative) component of velocity in the x direction.

To simplify the calculation, we rescale the incident wave, resulting in Eq. (C14) being

$$\psi(x, y) = \exp(ik_y y) \begin{cases} \left(\begin{matrix} 1 \\ \zeta_{I,1} \end{matrix} \right) \exp(\lambda_{I,1}x) + r \left(\begin{matrix} 1 \\ \zeta_{I,2} \end{matrix} \right) \exp(\lambda_{I,2}x) + \gamma r' \left(\begin{matrix} 1 \\ \zeta_{I,4} \end{matrix} \right) \exp(\lambda_{I,4}x), & x < 0, \\ a \left(\begin{matrix} 1 \\ \zeta_{II,1} \end{matrix} \right) \exp(\lambda_{II,1}x) + b \left(\begin{matrix} 1 \\ \zeta_{II,2} \end{matrix} \right) \exp(\lambda_{II,2}x) + c \left(\begin{matrix} 1 \\ \zeta_{II,3} \end{matrix} \right) \exp(\lambda_{II,3}x) + d \left(\begin{matrix} 1 \\ \zeta_{II,4} \end{matrix} \right) \exp(\lambda_{II,4}x), & 0 \leq x \leq D, \\ t \left(\begin{matrix} 1 \\ \zeta_{I,1} \end{matrix} \right) \exp(\lambda_{I,1}x) + \gamma t' \left(\begin{matrix} 1 \\ \zeta_{I,3} \end{matrix} \right) \exp(\lambda_{I,3}x), & D < x. \end{cases} \quad (\text{C15})$$

where $\gamma = \sqrt{\left| \frac{v_{g,x}}{v'_{g,x}} \right| \frac{\alpha_{3,4}}{\alpha_{1,2}}} = \sqrt{\left| \frac{v_{g,x}}{v'_{g,x}} \right| \cdot \frac{1+|\zeta_{I,1}|^2}{1+|\zeta_{I,3}|^2}}$. The only difference with Eq. (C10), mathematically, is that c' and d' are replaced by $\gamma r'$ and $\gamma t'$, respectively. It indicates that following the same approach of solving Eq. (C10), we can easily get parameters r , r' , t , and t' . Thus, the reflection (R) and transmission (T) probabilities can be calculated as $R = |r|^2 + |r'|^2$ and $T = |t|^2 + |t'|^2$.

4. Scenario of normal incidence

The normal incidence requires $v_y \equiv \frac{1}{\hbar} \frac{\partial E}{\partial k_y}$ to be 0. A sufficient condition is $k_y = 0$, which corresponds to the zeroth mode of energy bands. Denote $s = \text{sign}(E - V)$, then the eigenstate and corresponding wave modes are

$$\begin{aligned} \zeta_{1,2} &= \begin{pmatrix} \zeta_A \\ \zeta_B \end{pmatrix} = \frac{1}{2} \begin{pmatrix} 1-s \\ 1+s \end{pmatrix}, & \lambda_{x1,2} &= \pm i \arccos \left(1 - \frac{|E-V|}{2} \right), & \text{propagating,} \\ \zeta_{3,4} &= \begin{pmatrix} \zeta_A \\ \zeta_B \end{pmatrix} = \frac{1}{2} \begin{pmatrix} 1+s \\ 1-s \end{pmatrix}, & \lambda_{x3,4} &= \pm \text{arcosh} \left(1 + \frac{|E-V|}{2} \right), & \text{evanescent.} \end{aligned} \quad (\text{C16})$$

The wave function in Eq. (11) now is like Eq. (C10) as

$$\psi(x, y) = \frac{\exp(ik_y y)}{2} \times \begin{cases} \begin{pmatrix} 1-s \\ 1+s \end{pmatrix} \exp(\lambda_1^L x) + r \begin{pmatrix} 1-s \\ 1+s \end{pmatrix} \exp(\lambda_2^L x) + c' \begin{pmatrix} 1+s \\ 1-s \end{pmatrix} \exp(\lambda_3^L x), & x < 0, \\ a \begin{pmatrix} 1-s' \\ 1+s' \end{pmatrix} \exp(\lambda_1^M x) + b \begin{pmatrix} 1-s' \\ 1+s' \end{pmatrix} \exp(\lambda_2^M x) + c \begin{pmatrix} 1+s' \\ 1-s' \end{pmatrix} \exp(\lambda_3^M x) + d \begin{pmatrix} 1+s' \\ 1-s' \end{pmatrix} \exp(\lambda_4^M x), & 0 \leq x \leq D, \\ t \begin{pmatrix} 1-s \\ 1+s \end{pmatrix} \exp(\lambda_1^L x) + d' \begin{pmatrix} 1+s \\ 1-s \end{pmatrix} \exp(\lambda_4^L x), & D < x. \end{cases} \quad (\text{C17})$$

where $s = \text{sign}(E)$ and $s' = \text{sign}(E - V_s)$. Following the same approach, one can get parameters r , t and Eq. (12).

APPENDIX D: THE TUNNELING CONDUCTANCE VARIES WITH THE WIDTH OF THE BARRIER

Figure 6 shows how the relation between tunneling conductance G and the height of the barrier V_s varies as a function of the width of the barrier D . For positive V_s , the tunneling conductance has significant oscillation with respect to V_s , and the frequency is approximately in direct proportion to D , as does Fig. 3(b). This phenomenon indicates that the oscillation arises from the resonances and antiresonances between opposite propagating waves inside the barrier. For negative V_s , the tunneling conductance decreases exponentially no matter the value of D , which indicates the reflection is due to the opposite pseudospin orientations between incident and transmitted states.

-
- [1] B. Huard, J. A. Sulpizio, N. Stander, K. Todd, B. Yang, and D. Goldhaber-Gordon, Transport measurements across a tunable potential barrier in graphene, *Phys. Rev. Lett.* **98**, 236803 (2007).
- [2] R. V. Gorbachev, A. S. Mayorov, A. K. Savchenko, D. W. Horsell, and F. Guinea, Conductance of p - n - p graphene structures with “air-bridge” top gates, *Nano Lett.* **8**, 1995 (2008).
- [3] A. F. Young and P. Kim, Quantum interference and Klein tunnelling in graphene heterojunctions, *Nat. Phys.* **5**, 222 (2009).
- [4] N. Stander, B. Huard, and D. Goldhaber-Gordon, Evidence for Klein tunneling in graphene p - n junctions, *Phys. Rev. Lett.* **102**, 026807 (2009).
- [5] G. M. Rutter, S. Jung, N. N. Klimov, D. B. Newell, N. B. Zhitenev, and J. A. Stroscio, Microscopic polarization in bilayer graphene, *Nat. Phys.* **7**, 649 (2011).
- [6] K. F. Mak, C. H. Lui, J. Shan, and T. F. Heinz, Observation of an electric-field-induced band gap in bilayer graphene by infrared spectroscopy, *Phys. Rev. Lett.* **102**, 256405 (2009).
- [7] Y. Zhang, T.-T. Tang, C. Girit, Z. Hao, M. C. Martin, A. Zettl, M. F. Crommie, Y. Ron Shen, and F. Wang, Direct observation of a widely tunable bandgap in bilayer graphene, *Nature (London)* **459**, 820 (2009).
- [8] T. Ohta, A. Bostwick, T. Seyller, K. Horn, and E. Rotenberg, Controlling the electronic structure of bilayer graphene, *Science* **313**, 951 (2006).

- [9] A. B. Kuzmenko, I. Crassee, D. van der Marel, P. Blake, and K. S. Novoselov, Determination of the gate-tunable band gap and tight-binding parameters in bilayer graphene using infrared spectroscopy, *Phys. Rev. B* **80**, 165406 (2009).
- [10] L. M. Zhang, Z. Q. Li, D. N. Basov, M. M. Fogler, Z. Hao, and M. C. Martin, Determination of the electronic structure of bilayer graphene from infrared spectroscopy, *Phys. Rev. B* **78**, 235408 (2008).
- [11] I. Žutić, J. Fabian, and S. Das Sarma, Spintronics: Fundamentals and applications, *Rev. Mod. Phys.* **76**, 323 (2004).
- [12] F. Pullizzi, Spintronics, *Nat. Mater.* **11**, 367 (2012).
- [13] D. D. Awschalom and M. E. Flatté, Challenges for semiconductor spintronics, *Nat. Phys.* **3**, 153 (2007).
- [14] P. San-Jose, E. Prada, E. McCann, and H. Schomerus, Pseudospin valve in bilayer graphene: Towards graphene-based pseudospintronics, *Phys. Rev. Lett.* **102**, 247204 (2009).
- [15] Z. Bai, S. Zhang, Y. Xiao, M. Li, F. Luo, J. Li, S. Qin, and G. Peng, Controlling tunneling characteristics via bias voltage in bilayer graphene/WS₂/metal heterojunctions, *Nanomaterials* **12**, 1419 (2022).
- [16] M. I. Katsnelson, K. S. Novoselov, and A. K. Geim, Chiral tunnelling and the Klein paradox in graphene, *Nat. Phys.* **2**, 620 (2006).
- [17] J. R. Schaibley, H. Yu, G. Clark, P. Rivera, J. S. Ross, K. L. Seyler, W. Yao, and X. Xu, Valleytronics in 2D materials, *Nat. Rev. Mater.* **1**, 16055 (2016).
- [18] Z.-M. Yu, S. Guan, X.-L. Sheng, W. Gao, and S. A. Yang, Valley-layer coupling: A new design principle for valleytronics, *Phys. Rev. Lett.* **124**, 037701 (2020).
- [19] S. A. Vitale, D. Nezich, J. O. Varghese, P. Kim, N. Gedik, P. Jarillo-Herrero, Di Xiao, and M. Rothschild, Valleytronics: Opportunities, challenges, and paths forward, *Small* **14**, 1801483 (2018).
- [20] K. Wakabayashi and T. Aoki, Electrical conductance of zigzag nanographite ribbons with locally applied gate voltage, *Int. J. Mod. Phys. B* **16**, 4897 (2002).
- [21] J. Nakabayashi, D. Yamamoto, and S. Kurihara, Band-selective filter in a zigzag graphene nanoribbon, *Phys. Rev. Lett.* **102**, 066803 (2009).
- [22] W.-Y. He, Z.-D. Chu, and L. He, Chiral tunneling in a twisted graphene bilayer, *Phys. Rev. Lett.* **111**, 066803 (2013).
- [23] K. M. Masum Habib, R. N. Sajjad, and A. W. Ghosh, Chiral tunneling of topological states: Towards the efficient generation of spin current using spin-momentum locking, *Phys. Rev. Lett.* **114**, 176801 (2015).
- [24] M. Killi, S. Wu, and A. Paramekanti, Band structures of bilayer graphene superlattices, *Phys. Rev. Lett.* **107**, 086801 (2011).
- [25] C. Bai and X. Zhang, Klein paradox and resonant tunneling in a graphene superlattice, *Phys. Rev. B* **76**, 075430 (2007).
- [26] Z. F. Wang, Q. Li, Q. W. Shi, X. Wang, J. Yang, J. G. Hou, and J. Chen, Chiral selective tunneling induced negative differential resistance in zigzag graphene nanoribbon: A theoretical study, *Appl. Phys. Lett.* **92**, 133114 (2008).
- [27] C. Gutiérrez, L. Brown, C.-J. Kim, J. Park, and A. N. Pasupathy, Klein tunnelling and electron trapping in nanometre-scale graphene quantum dots, *Nat. Phys.* **12**, 1069-1075 (2016).
- [28] R. Du, M.-H. Liu, J. Mohrmann, F. Wu, R. Krupke, H. von Löhneysen, K. Richter, and R. Danneau, Tuning anti-Klein to Klein tunneling in bilayer graphene, *Phys. Rev. Lett.* **121**, 127706 (2018).
- [29] B. Van Duppen and F. M. Peeters, Four-band tunneling in bilayer graphene, *Phys. Rev. B* **87**, 205427 (2013).
- [30] W. Lu, W. Li, C. Xu, and Chengzhi Ye, Destruction of anti-Klein tunneling induced by resonant states in bilayer graphene, *J. Phys. D: Appl. Phys.* **48**, 285102 (2015).
- [31] L. Dell'Anna, P. Majari and M. R. Setare, From Klein to anti-Klein tunneling in graphene tuning the Rashba spinorbit interaction or the bilayer coupling, *J. Phys.: Condens. Matter* **30**, 415301 (2018).
- [32] Y. B-Ocampo, F. Leyvraz, and T. Stegmann, Electron optics in phosphorene *pn* junctions: Negative reflection and anti-super-Klein tunneling, *Nano Lett.* **19**, 7760 (2019).
- [33] G. Montambaux, L.-K. Lim, J.-N. Fuchs, and F. Piéchon, Wind-ing vector: How to annihilate two Dirac points with the same charge, *Phys. Rev. Lett.* **121**, 256402 (2018).
- [34] W. D. Wise, M. C. Boyer, K. Chatterjee, T. Kondo, T. Takeuchi, H. Ikuta, Y. Wang, and E. W. Hudson, Charge-density-wave origin of cuprate checkerboard visualized by scanning tunnelling microscopy, *Nat. Phys.* **4**, 696 (2008).
- [35] T.-S. Zeng, W. Zhu, and D. Sheng, Tuning topological phase and quantum anomalous Hall effect by interaction in quadratic band touching systems, *npj Quant. Mater.* **3**, 49 (2018).
- [36] H.-Q. Wu, Y.-Y. He, C. Fang, Z. Y. Meng, and Z.-Y. Lu, Diagnosis of interaction-driven topological phase via exact diagonalization, *Phys. Rev. Lett.* **117**, 066403 (2016).
- [37] K. Sun, Z. Gu, H. Katsura, and S. Das Sarma, Nearly flatbands with nontrivial topology, *Phys. Rev. Lett.* **106**, 236803 (2011).
- [38] K. Sun, H. Yao, E. Fradkin, and S. A. Kivelson, Topological insulators and nematic phases from spontaneous symmetry breaking in 2D Fermi systems with a quadratic band crossing, *Phys. Rev. Lett.* **103**, 046811 (2009).
- [39] A. MacKinnon, The calculation of transport properties and density of states of disordered solids, *Z. Phys. B* **59**, 385 (1985).
- [40] C. H. Lewenkopf and E. R. Mucciolo, The recursive Green's function method for graphene, *J. Comput. Electron* **12**, 203-231 (2013).
- [41] G. C. Papavassiliou, D. J. Lagouvardos, J. S. Zambounis, A. Terzis, C. P. Raptopoulou, K. Murata, N. Shirakawa, L. Ducasse, and P. Delhaes, Structural and physical properties of τ -(EDO-S, S-DMEDT-TTF)₂(AuBr₂)₁(AuBr₂)_y, *Mol. Cryst. Liq. Cryst.* **285**, 83 (1996).
- [42] T. Osada, Topological properties of τ -type organic conductors with a checkerboard lattice, *J. Phys. Soc. Jpn.* **88**, 114707 (2019).
- [43] T. Paananen and T. Dahm, Topological flat bands in optical checkerboardlike lattices, *Phys. Rev. A* **91**, 033604 (2015).
- [44] According to the anticommutation relation $\{H, \sigma_y\} = 0$ and the eigenfunction $H|\mathbf{k}s\rangle = E_{\mathbf{k}s}|\mathbf{k}s\rangle$, one can get $\langle \mathbf{k}s|H\sigma_y + \sigma_y H|\mathbf{k}s\rangle = 2E_{\mathbf{k}s}\langle \mathbf{k}s|\sigma_y|\mathbf{k}s\rangle = 0$ such that $\langle \mathbf{k}s|\sigma_y|\mathbf{k}s\rangle = 0$, for $E_{\mathbf{k}s} \neq 0$. Therefore, the pseudospin lies in the (*x-z*) plane.
- [45] Based on the Taylor expansion, we transform the trigonometric functions in $H_{\mathbf{k}}$ in the wave vector space into the operators in $\hat{H}_{\mathbf{k}}$ in the real space with redefining $\mathbf{k} = \hat{\mathbf{k}} - (\pi, \pi)$. For example, for

$$\begin{aligned}
 H_1 &= \cos(k_x) = 1 - \frac{k_x^2}{2!} + \frac{k_x^4}{4!} - o(k_x^4) \xrightarrow{\text{Fourier transformation}} \hat{H}_1 \\
 &= 1 - \frac{1}{2!}(-i\partial_x)^2 + \frac{1}{4!}(-i\partial_x)^4 - o[(-i\partial_x)^6],
 \end{aligned}$$

according to the Fourier transform of derivatives: $(ik)^n f(k) \rightarrow \frac{d^n}{dx^n} f(x)$. Then when the operator \hat{H}_1 acts on the wave function $\psi(x) = e^{i\lambda x}$, we obtain

$$\hat{H}_1 \psi(x) = \left[1 - \frac{1}{2!} \lambda^2 + \frac{1}{4!} \lambda^4 - o(\lambda^6) \right] \psi(x) = \cos(\lambda) \psi(x),$$

and here, we once again utilize the Taylor expansion.

- [46] J. Nilsson, A. H. Castro Neto, N. M. R. Peres, and F. Guinea Electron-electron interactions and the phase diagram of a graphene bilayer, *Phys. Rev. B* **73**, 214418 (2006).
- [47] E. McCann and V. I. Fal'ko Landau-level degeneracy and quantum Hall effect in a graphite bilayer, *Phys. Rev. Lett.* **96**, 086805 (2006).
- [48] I. Snyman and C. W. J. Beenakker, Ballistic transmission through a graphene bilayer, *Phys. Rev. B* **75**, 045322 (2007).
- [49] E. McCann and M. Koshino, The electronic properties of bilayer graphene, *Rep. Prog. Phys.* **76**, 056503 (2013).
- [50] A. H. Castro Neto, F. Guinea, N. M. R. Peres, K. S. Novoselov, and A. K. Geim, The electronic properties of graphene, *Rev. Mod. Phys.* **81**, 109 (2009).
- [51] Gerald D. Mahan, One dimension, *Quantum Mechanics in a Nutshell* (Princeton University Press, Princeton, 2009), Chap. 2.
- [52] S. Y. Lee, D. L. Duong, Q. A. Vu, Y. Jin, P. Kim, and Y. H. Lee, Chemically modulated band gap in bilayer graphene memory transistors with high on/off ratio, *ACS Nano* **9**, 9034 (2015).
- [53] W. S. Hwang, P. Zhao, S. G. Kim, R. Yan, G. Klimeck, A. Seabaugh, S. K. Fullerton-Shirey, H. G. Xing, and D. Jena Room-temperature graphene-nanoribbon tunneling field-effect transistors, *npj 2D. Mater. Appl.* **3**, 43 (2019).